Applied Surface Science 404 (2017) 180–187

Contents lists available at ScienceDirect

Applied Surface Science

journal homepage: www.elsevier.com/locate/apsusc

Full Length Article

Tensile loading induced phase transition and rippling in single-layer MoS_2

Hongwei Bao[a], Yuhong Huang[b], Zhi Yang[a], Yaping Miao[a,c], Paul K. Chu[c,*], Kewei Xu[a,d,*], Fei Ma[a,c,*]

[a] State Key Laboratory for Mechanical Behavior of Materials, Xi'an Jiaotong University, Xi'an, 710049 Shaanxi, China
[b] College of Physics and Information Technology, Shaanxi Normal University, Xi'an, 710062 Shaanxi, China
[c] Department of Physics and Materials Science, City University of Hong Kong,Tat Chee Avenue, Kowloon, Hong Kong, China
[d] Department of Physics and Opt-electronic Engineering, Xi'an University of Arts and Science, Xi'an, 710065 Shaanxi, China

ARTICLE INFO

Article history:
Received 13 October 2016
Received in revised form 13 January 2017
Accepted 25 January 2017
Available online 28 January 2017

Keywords:
MoS_2
Phase transition
Rippling
Molecular dynamics

ABSTRACT

Molecular dynamics (MD) simulation is performed to study the structural evolution of single-layer MoS_2 nanosheets under tensile loading and a phase transition from hexagonal structure to quadrilateral one is observed at a large strain when loaded along the zigzag direction but not along the armchair direction. Density functional theory (DFT) calculation illustrates that the newly generated quadrilateral phase is metallic. Further loading along the zigzag direction promotes an inhomogeneous distribution of lateral and shear stress around the phase boundaries due to local mechanical mismatch. As a result, periodic rippling parallel to the loading direction emerges and the wavelength and wave height change with strain according to $\lambda \sim \varepsilon^{-1/4}$ and $h \sim \varepsilon^{1/4}$. Accordingly, a graded distribution of strain can be produced or modulated by a simple tensile loading and the strategy might be utilized to enhance the photoelectrical properties of 2D materials and design strain-tunable nanodevices.

1. Introduction

Two-dimensional (2D) materials have become one of the research focuses in the fields of material science, physics, and chemistry in recent years [1]. In principle, any bulk materials with a laminated structure and bonded by van der Waals force can be exfoliated into graphene-like layers, including transition metal dichalcogenides (TMDs) [2], transition metal oxides [3], boron nitride [4], black phosphorus [5], and even artificially produced honeycomb structures [6]. There are more than 40 compounds in the family of TMDs and their physical properties vary from insulating to superconducting [7]. Hence, these types of materials have many potential applications in nano-electronics [8], photovoltaics [9], photo-catalysis [10], photo-detection [11], lithium ion battery [12], and nano-electromechanical systems (NEMS) [13].

It has been demonstrated that 2D materials can sustain an elastic strain of over 10% that is one order of magnitude larger than that of conventional materials and more importantly, the electronic, magnetic, optical and thermal properties can be tuned by strain. For instance, Guinea et al. [14] demonstrated quantized Landau-like electronic levels in graphene under strain at zero magnetic field and Mitchell et al. [15] found that an in-plane biaxial strain could induce polarization perpendicular to the sheets. Scalise et al. [16] showed that under tensile strain, the band gap of single-layer molybdenum disulfide ($SLMoS_2$) changed from direct to indirect and also decreased. Ding et al. [17] conducted molecular dynamics (MD) simulation to study the phonon spectra in multilayered MoS_2 and found that a compressive strain of 10% increased the thermal conductivity 10 times while a tensile strain of 5% reduced the thermal conductivity by 90%. Chen et al. [18] demonstrated that tensile strain enhanced the ferromagnetic stability of mono-layered $CrSiTe_3$ whereas compressive strain induced a ferromagnetic to anti-ferromagnetic transition. In particular, an elastic strain gradient can induce a continuous variation in the band gap. In this case, photons with different energies may be absorbed at different locations depending on band gap matching, and the photon-generated electron-hole pairs are swept towards the two sides by the appropriate band edge alignment so that they can be separated. This interesting property renders 2D materials unique solar energy funnels for light absorption, conveying, and concentration. Furthermore, Feng et al. [19] showed the possibility of producing elastic strain gradient through nanoindentation.

Although atomic force microscopy (AFM) and *in situ* tensile tests in conjunction with transmission electron microscopy (TEM) have been employed to measure the mechanical properties of 2D materi-

* Corresponding authors.
E-mail addresses: paul.chu@cityu.edu.hk (P.K. Chu), kwxu@mail.xjtu.edu.cn (K. Xu), mafei@mail.xjtu.edu.cn (F. Ma).

http://dx.doi.org/10.1016/j.apsusc.2017.01.263
0169-4332/

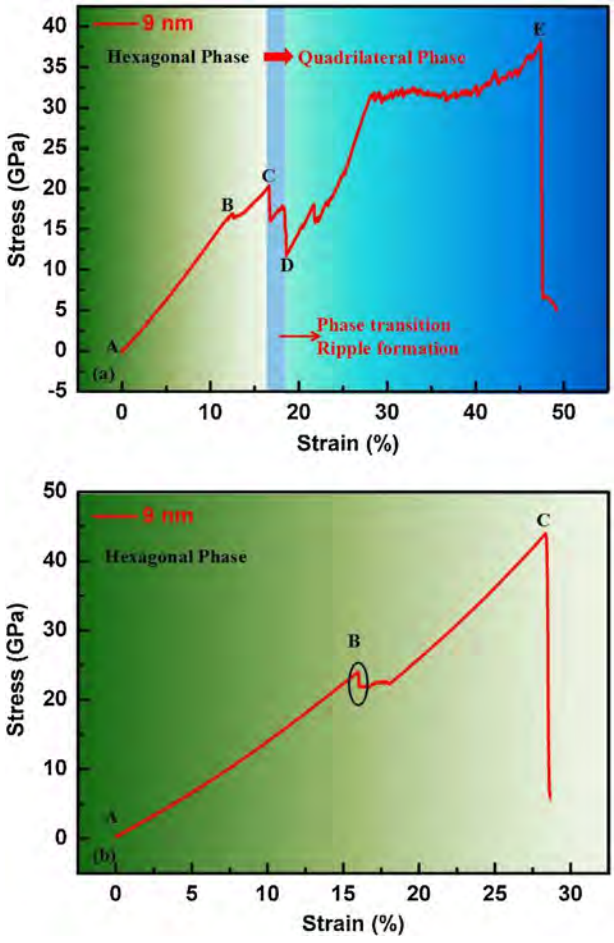

Fig. 1. Stress-strain curve of the 9 nm wide $SLMoS_2$ nanosheet under tensile loading: (a) Zigzag direction and (b) Armchair direction.

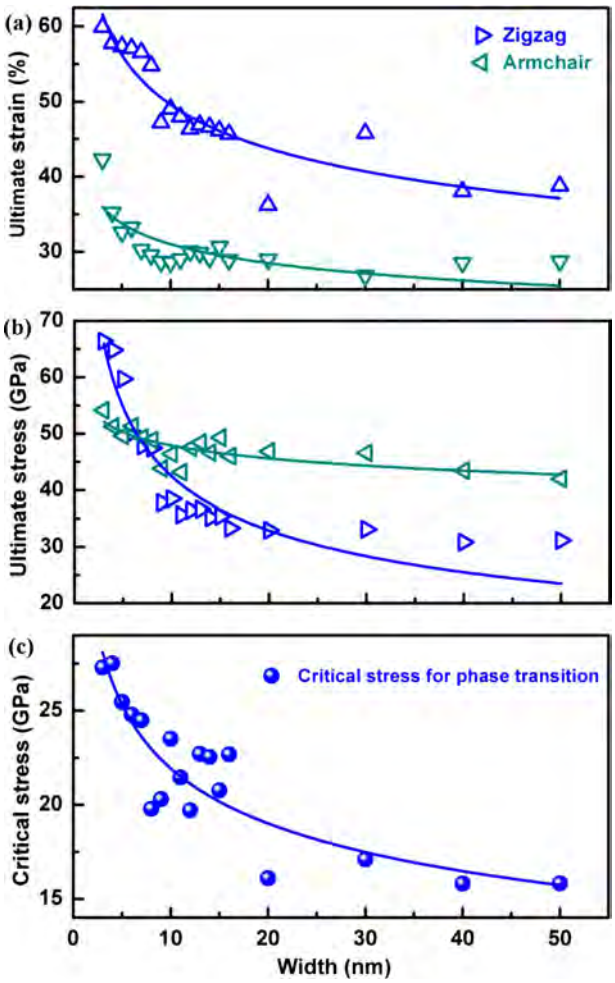

Fig. 2. (a) Ultimate strain and (b) Stress of the $SLMoS_2$ nanosheets loaded along the zigzag and armchair directions as a function of sheet widths; (c) Critical stress for the phase transition when loading is applied along the zigzag direction.

als, it is difficult to observe and characterize the structural evolution *in situ* [20]. In comparison, MD simulation is a reliable method to investigate the mechanical properties and structural evolution of 2D materials, and has been widely adopted to study the elastic modulus [21], intrinsic strength [22], defect behavior [23], and phase transformation [24]. The results are in good agreement with experimental ones as well as the results generated by the density functional theory (DFT) [25,26].

$SLMoS_2$ has a direct band gap of 1.8 eV and promising potential in next-generation field-effect transistors, optoelectronics, and energy harvesting devices [8–13]. $SLMoS_2$ has been fabricated by mechanical exfoliation and chemical vapor deposition (CVD) [27,28]. In the work by Zhao et al. [29], the phase transition from hexagonal structure to quadrilateral one and consequently rippling were evidenced when $SLMoS_2$ was loaded along zigzag direction below 40 K. They mainly focused on the temperature dependent behaviors. In this work, MD simulation is conducted to study the deformation behavior and structural evolution of $SLMoS_2$ under tensile loading. Stress-induced rippling is also observed and the features of ripples are quantitatively analyzed. The formation mechanism as well as the size dependence of rippling in $SLMoS_2$ is discussed accordingly.

2. Simulation model and method

In $SLMoS_2$, the Mo monolayer is sandwiched by two S monolayers and the Mo and S atoms are covalently bonded with each other. Based on a lattice constant of 2H-MoS_2 (a = 3.16 Å), the initial model of $SLMoS_2$ sheet with zigzag or armchair edges can be established [2,7–13,27–29]. There are commonly two types of zigzag edges in MoS_2 nano-sheets: one is Mo polar and the other is S polar. Some experimental and theoretical results demonstrated that zigzag edges with S termination are more stable, but the Mo polar edges passivated by S atoms are usually distorted [30–32]. However, S passivation affects the phase transition and rippling little, so S passivation is not considered. The $SLMoS_2$ nanosheets with dimensions between $3 \times 3\ nm^2$ and $50 \times 50\ nm^2$ are cut from the ideal infinite sheet. The periodic boundary conditions (PBCs) are applied in all directions and a vacuum region 30 Å in width along all directions is added to avoid the interactions of atoms near the opposite edges. LAMMPS (Large-scale Atomic/Molecular Massively Parallel Simulator) is used to conduct the MD simulation [33]. A new Stillinger-Webber (SW) potential developed by Jiang et al. [34,35] is adopted to describe the interatomic interactions, bond breaking, and bond reforming in $SLMoS_2$. An additional cut-off for the three-body interaction is embedded and bond stretching and angle rotation are described by the following relationships:

$$V_2 = Ae^{[\rho/r - r_{max}]}(B/r^4 - 1) \text{ and} \quad (1)$$

$$V_3 = Ae^{[\rho_1/(r_{12} - r_{max\,12}) + \rho_2/(r_{13} - r_{max\,13})]}(\cos\theta - \cos\theta_0)^2. \quad (2)$$

The simulated elastic properties, deformation behavior, thermal conductivity, and phonon spectrum based on the SW potential

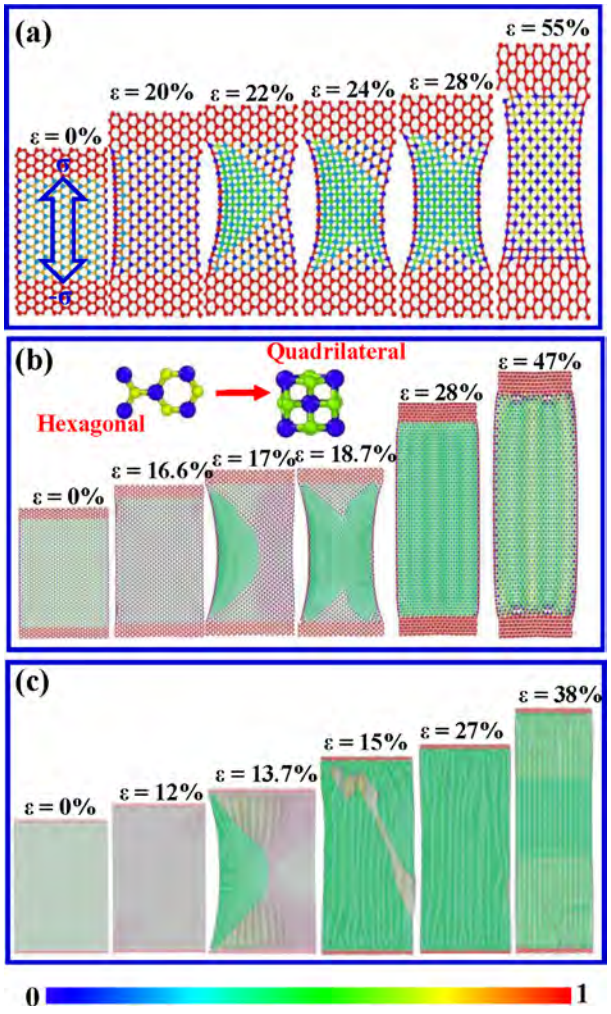

Fig. 3. Typical atomic configurations of the $SLMoS_2$ nanosheets with different widths under tensile loading along the zigzag direction: (a) 3 nm; (b) 9 nm, and (c) 50 nm.

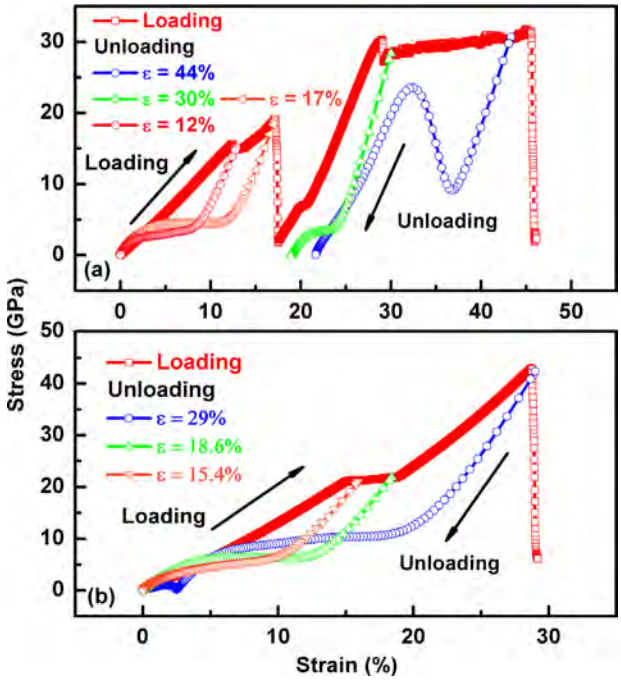

Fig. 4. Stress-strain curves of $SLMoS_2$ nanosheet with a width of 15 nm loaded along (a) zigzag direction and (b) armchair direction, and unloaded from different strain.

show good agreement with the DFT and experimental results [35,36].

The initial $SLMoS_2$ nanosheets are relaxed in the NPT (number of atoms N, pressure P, and temperature T are constant) ensemble at T = 10 K and P = 0 Pa for 2 ns and the nanosheets are thermally equilibrated using the Nosé-Hoover thermostat [37,38]. The temperature is controlled using the Nosé-Hoover thermostat. The test results show that both the potential energy and the temperature are converged at 1 ns, and the optimized atomic configuration is obtained. So the selected ensemble and relaxation time is good for the MD simulation. The standard Newton equations of atomic motion are integrated using the velocity Verlet algorithm with a time step of 1 fs, and the uniaxial tensile loading is applied by uniformly displacement of lattice in the nanosheets. The two edges parallel to the loading direction are free to relax but the other two edges perpendicular to the loading direction are clamped. A strain increment of 0.01% is applied in each time step, corresponding to a strain rate of $10^8\ S^{-1}$. The strain rate is low enough to guarantee the sheet is in equilibrium. The atomic stress is calculated using the virial definition [39],

$$\sigma_{ij} = \frac{1}{V}\left(\frac{1}{2}\sum_{\alpha=1}^{N}\sum_{\beta\neq\alpha}^{N} U'\left(\gamma^{\alpha\beta}\frac{\Delta x_i^{\alpha\beta}\Delta x_j^{\alpha\beta}}{\gamma^{\alpha\beta}} - \sum_{\alpha=1}^{N} m_\alpha \dot{x}_i^{\alpha}\dot{x}_j^{\beta}\right)\right), \qquad (3)$$

where V is the total volume of the $SLMoS_2$ nanosheets with a thickness of 0.61 nm [40], N is the total number of atoms, $\dot{x}_i^{\alpha}$ is the ith component of the velocity of atom α, $\Delta x_j^{\alpha\beta} = \dot{x}_j^{\alpha} - \dot{x}_j^{\beta}$, m_α is the mass of atom α, $\gamma^{\alpha\beta}$ is the distance between atoms α and β and U' is the potential energy function. In Lammps, there are 6 components in the symmetric stress tensor: σ_{xx}, σ_{yy}, σ_{zz}, σ_{xy}, σ_{xz} andσ_{yz}, of which σ_{zz}, $\sigma_{xz}$and σ_{yz} is negligible for 2D materials. If the tensile loading is along x axis, the tensile stress is calculated by summing the stress tensor component σ_{xx} of each atom and, the lateral stress and shear stress are calculated by summing the stress tensor components σ_{yy} and σ_{xy}, respectively. The atomic structures at different time are visualized by the OVITIO package [41].

DFT implemented in MedeA-VASP is conducted to calculate the band structure and electronic states. The generalized gradient approximation with the Perdew–Burke–Ernzerhof exchange–correlation potential (GGA-PBE) is used with a kinetic-energy cut off of 480 eV. Brillouin-zone integration is carried out with a $11 \times 11 \times 1$ k-mesh according to the Mon-khorst-Pack scheme [42,43].

3. Results and discussion

Fig. 1(a) and (b) shows the stress-strain curves of 9 nm wide $SLMoS_2$ nanosheets under tensile loading along the zigzag and armchair directions, respectively. As shown in Fig. 1(a), when the tensile loading is applied along the zigzag direction, the stress changes with strain linearly up to a strain of about 12.6% (A → B), corresponding to elastic deformation of the hexagonal lattice. Subsequently, a small drop in stress emerges at point B as a result of displacement of atoms, but the stress is further increased up to 16.68 GPa at a strain of 16.6%. Afterwards, the stress drops abruptly (C → D) as a result of the phase transition from hexagonal to quadrilateral and it will be discussed later according to the structural evolution. The phase transition is complete at a strain of 18.9% accompanied by a sudden drop in potential energy. Further tensile loading leads to the stretching and rippling of the newly formed phase (D → E). As shown in Fig. 1(b), when the tensile loading is

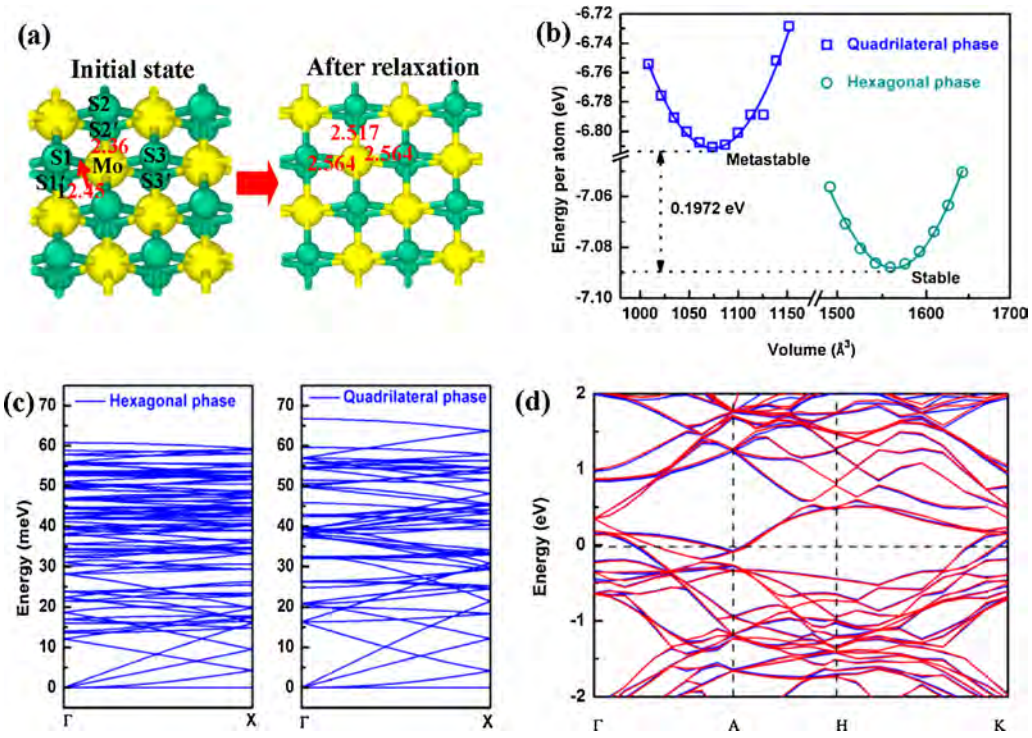

Fig. 5. (a) Initial and relaxed quadrilateral model of $SLMoS_2$; (b) the average energy per atom of hexagonal and quadrilateral phases as a function of volume; (c) Phonon band structure of these two phases; (d) Band structure of the quadrilateral phase.

applied along the armchair direction, elastic deformation occurs in the strain range of 0%–16% (A → B). After a small stress drop at a strain of 16%, the stress increases with strain continuously until fracture (B → C). However, the aforementioned phase transition does not take place and the potential energy increases continuously with strain until destructive fracture. That is, the tensile loading induced phase transition is sensitive to the direction.

The ultimate strain and stress just before fracture are two important parameters describing the resistance of materials to external force. As shown in Fig. 2(a) and (b), as the sheet width is reduced from 50 nm to 3 nm, the ultimate strain and stress along the armchair direction increases from 29% to 42% by 44.8% and from 42 GPa to 54 GPa by 28.6%, while the ultimate strain and stress along zigzag direction increases from 39% to 60% by 53.8% and from 31 GPa to 67 GPa by 116%. The fitted relationship between the ultimate stress (σ) and sheet width (w) are $\sigma = 98.66\, w^{-0.37}$ and $\sigma = 56.3\, w^{-0.07}$ along the zigzag and armchair directions, respectively. This behavior is similar to that observed from conventional metals, i.e., "the smaller, the stronger" [44]. The remarkable enhancement in mechanical strength along zigzag direction is related to the aforementioned phase transformation. Fig. 2(c) shows the critical stress required for the phase transition along the zigzag direction. It increases from 15.82 GPa to 27.3 GPa by 72% as the sheet width is reduced from 50 nm to 3 nm. Hence, the smaller the sheet width, the more difficult it is for the phase transition from hexagonal to quadrilateral.

Fig. 3(a)–(c) shows the typical snapshots of the atomic configurations of the $SLMoS_2$ nanosheets with widths of 3 nm, 9 nm, and 50 nm, respectively, when loaded along the zigzag direction. The atoms are colored by the potential energy per atom and processed by the OVITO package. The red regions denote the clamped boundaries. It can be seen that the quadrilateral phase nucleates from the sheet edges due to the higher energy when the applied strain exceeds a critical value (20%, 16.6% and 12% for the nanosheets with widths of 3 nm, 9 nm, and 50 nm, respectively). This corresponds to a sudden drop in the stress as shown in Fig. 1(a). The phase transition sweeps through the nanosheets with increasing strain and the newly generated quadrilateral phase is indicated in green. This phase transition from hexagonal structure to quadrilateral one was also observed in $SLMoS_2$ when loaded along zigzag direction at the temperature lower than 40 K and under nano-indentation at 10 K [29,37]. Similar structural transitions from wurtzite to graphite-like phase and body-centered-tetragonal phase (BCT-4) took place in ZnO, GaN, ZnS, and MgO nanowires under tensile loading [45–48]. The inset in Fig. 3(b) schematically shows the atomic configurations of the hexagonal and quadrilateral phases. During phase transition, the bond lengths of S-Mo vary from the initial value of 2.40 Å to 2.45 Å by 2.1% and 2.36 Å by 1.67%, respectively. In fact, as the applied strain is increased, the system energy increases especially for atoms at the edges. Nearly all the phase transitions are activated from the S-polar edge but not from Mo-polar edge even with S passivated. Owing to the thermal fluctuation, the atoms at the edges are displaced from their equilibrium positions towards neighboring Mo atoms at a large strain thereby facilitating the formation of the quadrilateral phase.

In order to confirm the structural stability of the newly produced quadrilateral phase, taking the $SLMoS_2$ nanosheet with a width of 15 nm as an example, unloading process is also simulated by releasing the stress from a given strain. Fig. 4(a) shows the stress-strain curves of the $SLMoS_2$ nanosheet loaded along zigzag direction and unloaded from different strains. If the $SLMoS_2$ nanosheet is unloaded from a strain at which the phase transition does not take place, for example, from 12% and 17%, the deformation is completely reversible. However, a residual strain of about 21% is observed if the $SLMoS_2$ nanosheet is unloaded from a strain of 30% and 44% at which the phase transition has already occurred. Thermodynamically, the newly formed quadrilateral phase is indeed metastable and it is difficult to recover to the initial hexagonal phase because of an energy barrier of 0.1972 eV per atom. Similar results were evidenced previously, that is, the quadrilateral structure was induced under tensile loading along zigzag direction and the original hexagonal phase cannot be recovered with a

residual strain of 20% or so after unloading [29]. Fig. 4(b) shows the stress-strain curves of $SLMoS_2$ nanosheet loaded along armchair direction and unloaded from different strains. The hexagonal lattice is elongated during tensile loading and is completely reversible upon unloading even from a strain of 29%. The energy loss leads to the hysteretic loops in stress-strain curves.

First-principles calculations are conducted to study the structural stability, energy band structure and the electronic states of the new quadrilateral phase as well as the initial hexagonal phase. Fig. 5(a) displays the initial atomic model (left) in the quadrilateral lattice which is constructed according to the MD results and relaxed model (right). In the initial model, the bond length of Mo-S1, Mo-S3, and Mo-S2′ is set at 2.45 Å and that of Mo-S1′, Mo-S3′ and Mo-S2 is 2.36 Å. A 1.5 nm thick vacuum layer is added to the top of the $SLMoS_2$ to avoid the interactions between layers. After completely relaxed, the bond length of Mo-S1, Mo-S3, and Mo-S2′ is stretched into 2.564 Å and that of Mo-S1′, Mo-S3′ and Mo-S2 is 2.517 Å. The average energy per atom of these two phases as a function of volume is calculated. As shown in Fig. 5(b), there is a minimum energy at a volume of 1069.48 $Å^3$ and 1559.27 $Å^3$ for the quadrilateral and hexagonal phases, respectively, moreover, the average energy per atom in the quadrilateral phase at equilibrium state is about 0.1972 eV higher than that in hexagonal phase. Hence, the initial hexagonal phase is stable and the newly quadrilateral phase is metastable. Fig. 5(c) shows the phonon dispersion curves of the two phases calculated by using MD simulation in which the atomic interaction is described by the SW potential. No imaginary frequency can be identified, indicating that the quadrilateral phase is dynamically stabilized. Fig. 5(d) shows the band structure of the newly quadrilateral phase without the spin-orbit coupling (SOC) (red lines) and with SOC (blue lines), in which the Fermi level is set at 0 eV. Apparently, the SOC hardly affects the band structure, and there are concentrated electronic states around the Fermi level, and no band gap can be induced, characteristic of metals. Hexagonal $SLMoS_2$ is a typical semiconductor with a large band gap of about 1.8 eV and the band gap will be substantially reduced under tensile loading [8–13]. A uniaxial tensile strain of about 11% will close the band gap, resulting in a semiconductor-to-metal transition [14,15]. If the uniaxial strain is further increased up to about 16.6%, a structural transformation from hexagonal to quadrilateral occurs but the $SLMoS_2$ nanosheets maintain metallic features.

Fig. 6(a)–(c) shows the typical snapshots of the atomic configurations of the 3 nm, 9 nm, and 50 nm wide $SLMoS_2$ nanosheets, respectively, when loading is applied along the armchair direction. The quadrilateral phase is only observed from some local regions in the 3 nm wide $SLMoS_2$ nanosheet at a strain of over 30%. As for the wider $SLMoS_2$ nanosheets, tensile loading only leads to stretching of the S-Mo bonds and the hexagonal lattice is maintained as shown in the inset in Fig. 6(c).

Following the phase transition, periodic rippling parallel to the loading direction usually takes place in $SLMoS_2$ nanosheets that are wide enough, as shown in Fig. 3. Fig. 7(a)–(c) presents the typical snapshots of the cross-sectional atomic configurations of the 3 nm, 9 nm, and 50 nm wide $SLMoS_2$ nanosheets, respectively. As shown in Fig. 7(a), the 3 nm $SLMoS_2$ nanosheet is always flat even after phase transition at a strain of 22% and further loaded to a strain of 55%. In contrast, periodic rippling occurs in the 9 nm and 50 nm $SLMoS_2$ nanosheets immediately after the phase transition is initiated and rippling is gradually extended throughout the sheets with increasing strain, as shown in Fig. 7(b) and (c). Fig. 8(a) and (b) shows the ripple wavelength (λ) and wave height (h) of the three $SLMoS_2$ nanosheets at different tensile strains. In fact, when the $SLMoS_2$ nanosheets are less than 9 nm, rippling is not observed. Taking the 3 nm wide $SLMoS_2$ nanosheet as an example and as shown in Fig. 8(a) and (b), λ is always zero and h is nearly constant with increasing strain. However, for the 9 nm $SLMoS_2$ nanosheets,

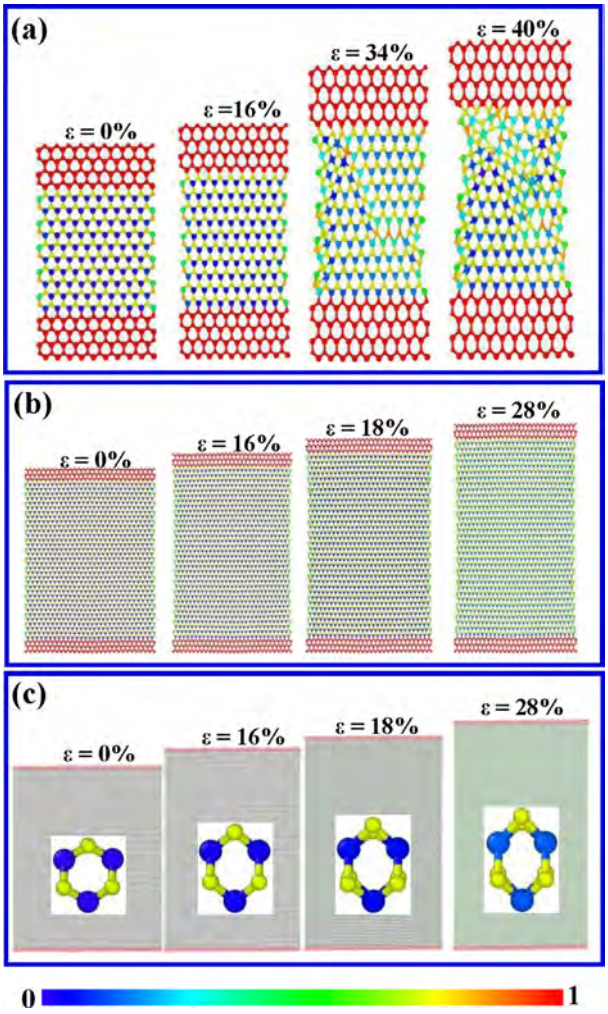

Fig. 6. Typical atomic configurations of the $SLMoS_2$ nanosheets with different widths under tensile loading along the armchair direction: (a) 3 nm; (b) 9 nm, and (c) 50 nm.

both λ and h increase sharply after a critical strain at which the phase transition is initiated and then they change slightly with increasing strain when the phase transition is completed. The rippling characteristics depend on the size of $SLMoS_2$. Fig. 8(c) shows the maximal λ and h as a function of sheet width. The values of λ and h are zero for the nanosheets smaller than 9 nm, indicating that the smaller $SLMoS_2$ nanosheets can stay flat even under large tensile strain. As the sheet width is increased from 9 nm to 50 nm, λ increases from 2.62 nm to 4.41 nm by 68.3% and h increases from 0.66 nm to 1.14 nm by 72.7%. The dependence of the wavelength and wave height of the ripples on the tensile strain can be described by the Föppl von Kármán equations [49–51]:

$$\lambda = \sqrt{\frac{2\pi l t}{\sqrt{3(1-\nu^2)\varepsilon}}} \quad \text{and} \tag{4}$$

$$h = \frac{\sqrt{2(1-\nu)}\gamma}{\pi}\lambda = \sqrt{\frac{2lt}{\pi}\sqrt{\frac{(1-\nu)\varepsilon}{3(1+\nu)}}}. \tag{5}$$

in which l is the width of a thin sheet, t is the sheet thickness, the Poisson's ratio ν of 0.267 is calculated by the DFT method and ε is the longitudinal strain [26,36]. Eqs. (4) and (5) can be simplified as $\lambda \sim \varepsilon^{-1/4}$ and $h \sim \varepsilon^{1/4}$, respectively. Fig. 9(a) and (b) displays the fitted relationship of λ versus $\varepsilon^{-1/4}$ and h versus $\varepsilon^{1/4}$ for the 9 nm, 16 nm,

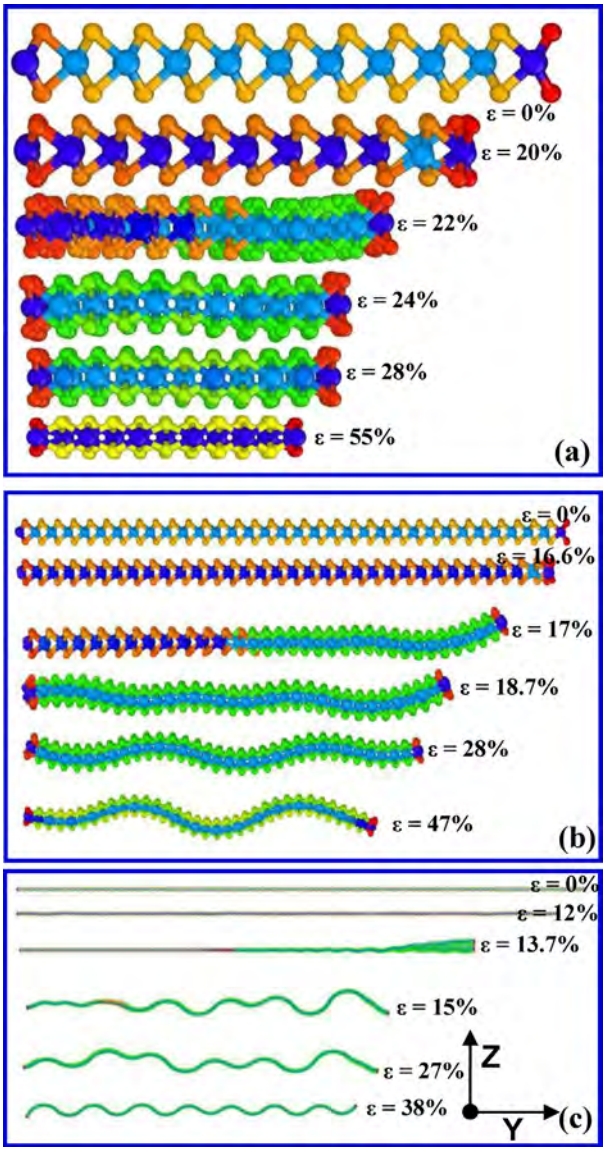

Fig. 7. Ripple configurations with lateral section of the $SLMoS_2$ nanosheets with different widths under tensile loading along the zigzag direction: (a) 3 nm; (b) 9 nm, and (c) 50 nm.

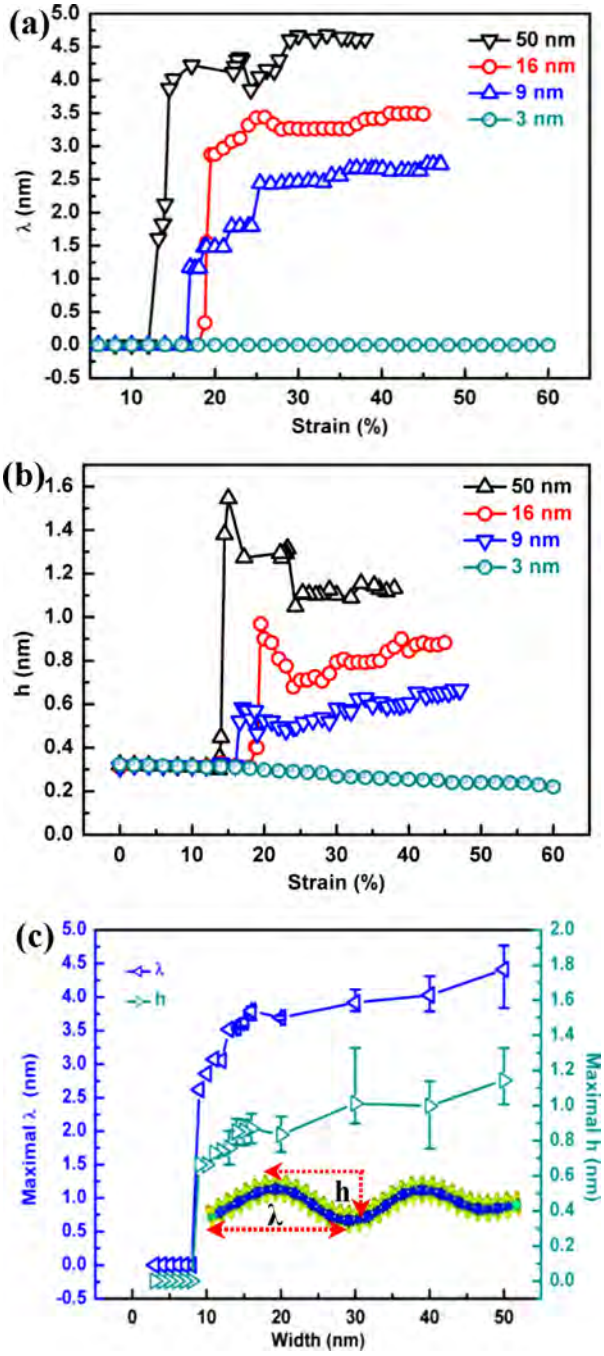

Fig. 8. (a) Rippling wavelength and (b) Wave height as a function of strain; (c) Rippling wavelengths and heights in the zigzag $SLMoS_2$ nanosheets with different widths.

and 50 nm $SLMoS_2$ nanosheets and the good linear fits indicate the validity of the continuum theory for thin sheets with a nanoscale.

Taking the 50 nm $SLMoS_2$ nanosheet as an example, Fig. 10(a), (c), (e), (g), and (i) show the evolution of the ripple profiles in the *xoy* plane at strains of 0%, 13.7%, 17.2%, 27%, and 38%. It is colored according to the out-of-plane displacement of atoms. The ripples are formed initially at the interface between the hexagonal and quadrilateral phases [Fig. 10(c)] and then propagate and merge with each other [Fig. 10(e)]. Upon further tensile loading, the ripples become periodical and regular [Fig. 10(g) and (i)]. Fig. 10(b), (d), (f), (h), and (j) display the profiles of ripples along the solid light brown lines in the left panels of Fig. 10. The ripple profiles can be well fitted by sinusoidal functions, as highlighted by the solid blue lines in the right panels of Fig. 10. The results resemble stretch-induced wrinkling of thin elastic sheets with a macroscale [49–51]. The clamped boundaries prevent the sheets from contracting laterally in the local regions and the shear stress emerges near the boundaries thereby produces wrinkling. Wrinkling and rippling induced by the thermal effect, shear and compression have been observed from graphene and phosphorene nanosheets [52,53]. As for 2D materials, the Poisson's effect becomes substantial, that is, when the nanosheets are tensile loaded along one direction, the other in-plane direction will be compressed, resulting in the shorted width, as shown in Fig. 7. However, lateral compressive stress during tensile loading process is too small to induce ripples in $SLMoS_2$ nanosheets. In fact, stress gradient emerges around the phase boundaries between the hexagonal structure and the quadrilateral structure in $SLMoS_2$ nanosheets. The inhomogeneous stress distribution around the phase boundaries may be the driving force for the formation of ripples on $SLMoS_2$ nanosheets. Fig. 11(a) and (b) shows the lateral and shear stress distributions in the 50 nm $SLMoS_2$ nanosheets during phase transition. As shown in Fig. 11(a), the lateral stress in the quadrilateral phase domain is positive (ten-

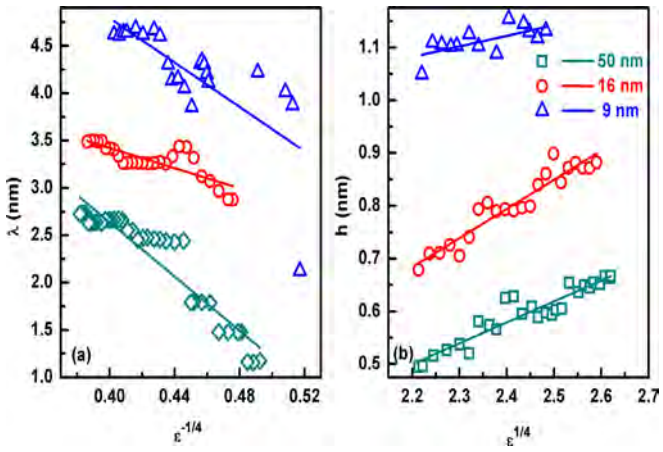

Fig. 9. Wavelength and wave height versus $\varepsilon^{1/4}$ with the symbols representing the simulation results and solid lines standing for the best-fitted curves.

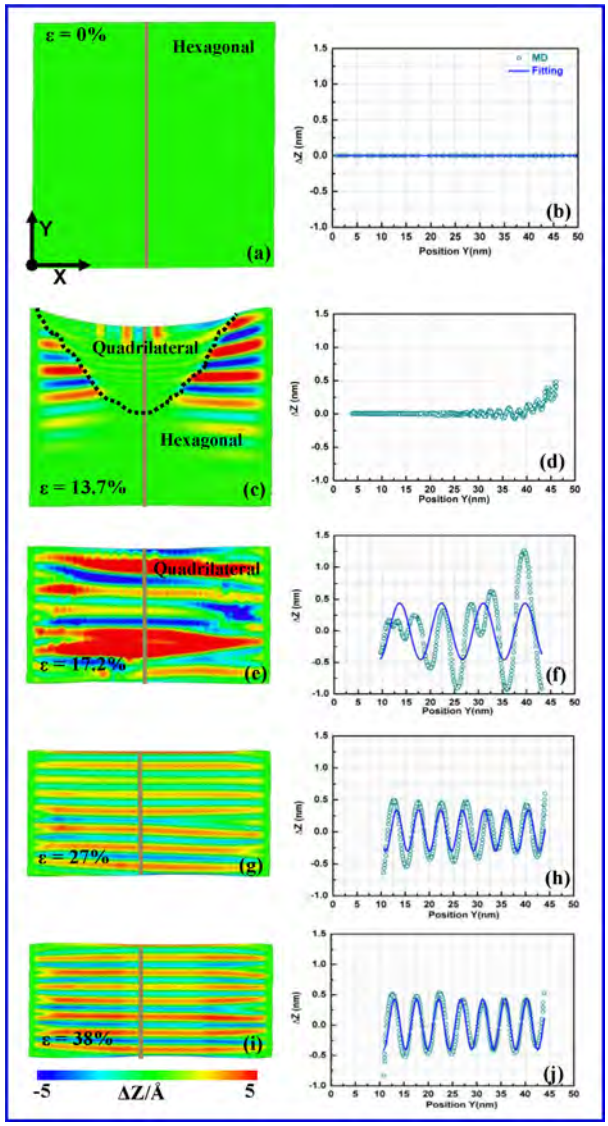

Fig. 10. (a), (c), (e), (g), and (i) Ripple patterns of the 50 nm wide $SLMoS_2$ nanosheet at strains of 0%, 13.7%, 17.2%, 27% and 38%; (b), (d), (f), (h), (j) Out-of-plane displacement along the solid light brown lines in the left panels. The ripple profiles can be well fitted by sinusoidal functions.

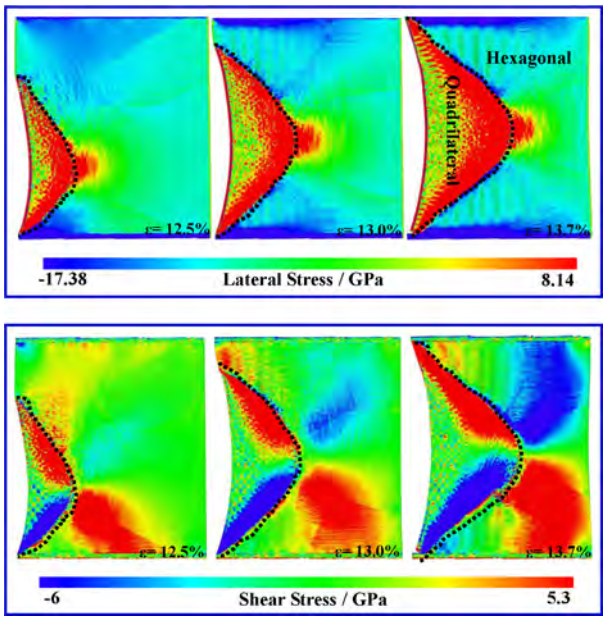

Fig. 11. (a) Lateral stress and (b) Shear stress distributions in the 50 nm wide $SLMoS_2$ nanosheet at tensile strains of 12.5%, 13.0%, and 13.7%.

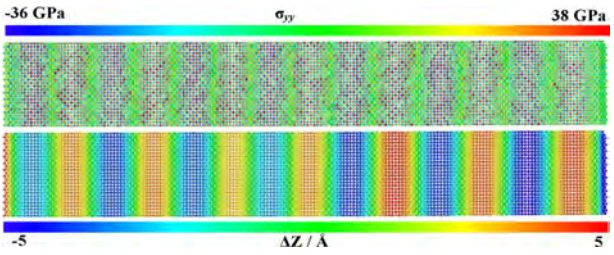

Fig. 12. Lateral atomic stress distribution and out-of-plane displacement distribution in the 50 nm wide $SLMoS_2$ nanosheet at a strain of 27%.

sile) but negative (compressive) in the hexagonal phase domain. As shown in Fig. 11(b), the shear stress is anti-symmetrically distributed around the phase boundary and it is butterfly-like with one branch having positive shear stress and the other having negative shear stress. The inhomogeneous distributed lateral and shear stresses around the phase boundary promote rippling. As for the nanosheets with a small width (<9 nm), the stress is also inhomogeneously distributed around the phase boundaries. But the phase domain is too small to bend along the width direction, and thus the aforementioned ripples cannot be found. Fig. 12 shows the lateral stress distribution in the 50 nm $SLMoS_2$ nanosheet at a tensile strain of 27%. The strain gradient is obvious and the inhomogeneous strain distribution may shift the band edges of MoS_2 nanosheets thus affecting the physical properties. In fact, recent theoretical calculation by DFT and tight-binding (TB) methods has demonstrated that ripples may reduce the bandgap and enhance the electronic and optical properties [42,43].

4. Conclusion

The tensile deformation process in $SLMoS_2$ nanosheets with different widths along the zigzag and armchair directions is studied by MD simulation. The hexagonal to quadrilateral phase transition is observed at a large strain when loading is applied along the zigzag direction but not along the armchair direction. DFT calculation illustrates that the new phase is stable and metallic and tensile loading transforms the MoS_2 from semiconducting to metallic. The

ultimate stress and strain increase with decreasing widths when loading is applied along both the zigzag and armchair directions. Further loading along the zigzag direction promotes the inhomogeneous distribution of lateral and shear stress around the phase boundaries in the nanosheets with a large width. As a result, periodic rippling perpendicular to the loading direction emerges and the wavelength and the wave height change with strain according to $\lambda \sim \varepsilon^{-1/4}$ and $h \sim \varepsilon^{1/4}$. In this way, a graded strain distribution can be produced or modulated by tensile loading and this phenomenon can be exploited to enhance the photoelectric properties of 2D materials and design strain-tunable nanodevices.

Acknowledgements

This work was jointly supported by National Natural Science Foundation of China (Grant No. 51471130), Fundamental Research Funds for the Central Universities and City University of Hong Kong Applied Research Grant (ARG) No. 9667104.

References

[1] M. Xu, T. Liang, M. Shi, H. Chen, Graphene-like two-dimensional materials, Chem. Rev. 113 (2013) 3766–3798.
[2] C. Ataca, H. Şahin, S. Ciraci, Single-layer MX_2 transition-metal oxides and dichalcogenides in a honeycomb-like structure, J. Phys. Chem. C 116 (2012) 8983–8999.
[3] L.F. Li, Y.L. Wang, S.Y. Xie, X.B. Li, Y.Q. Wang, R.T. Wu, H.B. Sun, S.B. Zhang, H.J. Gao, Two-dimensional transition metal honeycomb realized: Hf on Ir (111), Nano Lett. 13 (2013) 4671–4674.
[4] C. Jin, F. Lin, K. Suenaga, S. Iijima, Fabrication of a freestanding boron nitride single layer and its defect assignments, Phys. Rev. Lett. 102 (2009) 195505.
[5] J.R. Brent, N. Savjani, E.A. Lewis, S.J. Haigh, D.J. Lewis, P. O'Brien, Production of few-layer phosphorene by liquid exfoliation of black phosphorus, Chem. Commun. 50 (2014) 13338–13341.
[6] L. Meng, Y.L. Wang, L.Z. Zhang, S.X. Du, R.T. Wu, L.F. Li, Y. Zhang, G. Li, H.T. Zhou, W.A. Hofer, Buckled silicene formation on Ir (111), Nano Lett. 613 (2013) 685–690.
[7] M. Chhowalla, H.S. Shin, G. Eda, L.J. Li, K.P. Loh, H. Zhang, The chemistry of two-dimensional layered transition metal dichalcogenide nanosheets, Nat. Chem. 5 (2013) 263–275.
[8] K.F. Mak, C. Lee, J. Hone, J. Shan, T.F. Heinz, Seeing many-body effects in single- and few-layer graphene: observation of 2-dimensional saddle point excitons, Phys. Rev. Lett. 105 (2010) 136805.
[9] R.S. Sundaram, M. Engel, A. Lombardo, R. Krupke, A.C. Ferrari, P. Avouris, M. Steiner, Electroluminescence in single layer MoS_2, Nano Lett. 13 (2013) 1416–1421.
[10] Z. Wu, B. Fang, Z. Wang, C. Wang, Z. Liu, F. Liu, W. Wang, A. Alfantazi, D. Wang, D.P. Wilkinson, MoS_2 nanosheets: a designed structure with high active site density for the hydrogen evolution reaction, ACS Catal. 3 (2013) 2101–2107.
[11] M. Fontana, T. Deppe, A.K. Boyd, M. Rinzan, A.Y. Liu, M. Paranjape, P. Barbara, Electron–hole transport and photovoltaic effect in gated MoS_2 Schottky junctions, Sci. Rep. 3 (2013) 1634.
[12] M. Shanmugam, C.A. Durcan, B. Yu, Layered semiconductor molybdenum disulfide nanomembrane based Schottky-barrier solar cells, Nanoscale 4 (2012) 7399–7405.
[13] K.F. Mak, K.L. McGill, J. Park, P.L. McEuen, The valley hall effect in MoS_2 transistors, Science 344 (2014) 1489–1492.
[14] F. Guinea, M.I. Katsnelson, A.K. Geim, Energy gaps and a zero-field quantum hall effect in graphene by strain engineering, Nat. Phys. 6 (2010) 30–33.
[15] T.O. Mitchell, J.R. Evan, Engineered piezoelectricity in graphene, ACS Nano 6 (2011) 1387–1394.
[16] E. Scalise, M. Houssa, G. Pourtois, V. Afanas'ev, A. Stesmans, Strain-induced semiconductor to metal transition in the two-dimensional honeycomb structure of MoS_2, Nano Res. 5 (2012) 43–48.
[17] Z.W. Ding, J.W. Jiang, Q.X. Pei, Y.W. Zhang, In-plane and cross-plane thermal conductivities of molybdenum disulfide, Nanotechnology 26 (2015) 065703.
[18] X.F. Chen, J.S. Qia, D.N. Shi, Strain-engineering of magnetic coupling in two-dimensional magnetic semiconductor $CrSiTe_3$: competition of direct exchange interaction and super exchange interaction, Phys. Lett. A 379 (2015) 60–63.
[19] J. Feng, X. Qian, C.W. Huang, J. Li, Strain-engineered artificial atom as a broad-spectrum solar energy funnel, Nat. Photonics 6 (2012) 866–872.
[20] S. Bertolazzi, J. Brivio, A. Kis, Stretching and breaking of ultrathin MoS_2, ACS Nano 5 (2011) 9703–9709.
[21] T.Y. Zhang, Z.J. Wang, W.K. Chan, Eigenstress model for surface stress of solids, Phys. Rev. B 81 (2010) 195427.
[22] F. Ma, Y.J. Sun, D.Y. Ma, K.W. Xu, P.K. Chu, Reversible phase transformation in graphene nano-ribbons: lattice shearing based mechanism, Acta Mater. 59 (2011) 6783–6789.
[23] E. Martínez, A. Caro, I.J. Beyerlein, Atomistic modeling of defect-induced plasticity in CuNb nanocomposites, Phys. Rev. B 90 (2014) 054103.
[24] F. Ma, K.W. Xu, P.K. Chu, Surface-induced structural transformation in nanowires, Mater. Sci. Eng. R 74 (2013) 173–209.
[25] R. Agrawal, B. Peng, E.E. Gdoutos, H.D. Espinosa, Elasticity size effects in ZnO nanowires–a combined experimental-computational approach, Nano Lett. 8 (2008) 3668–3674.
[26] R.C. Cooper, C. Lee, C.A. Marianetti, X.D. Wei, J. Hone, J.W. Kysar, Nonlinear elastic behavior of two-dimensional molybdenum disulfide, Phys. Rev. B 87 (2013) 035423.
[27] D.M. Tang, D.G. Kvashnin, S. Najmaei, Y. Bando, K. Kimoto, P. Koskinen, P.M. Ajayan, B.I. Yakobson, P.B. Sorokin, J. Lou, D. Golberg, Nanomechanical cleavage of molybdenum disulphide atomic layers, Nat. Commun. 5 (2014) 4631.
[28] A. Splendiani, L. Sun, Y. Zhang, T. Li, J. Kim, C.Y. Chim, G. Galli, F. Wang, Emerging photoluminescence in monolayer MoS_2, Nano Lett. 10 (2010) 1271–1275.
[29] J.H. Zhao, L.Z. Kou, J.W. Jiang, T. Rabczuk, Tension-induced phase transition of single layer molybdenum disulphide (MoS_2) at low temperatures, Nanotechnology 25 (2014) 295701.
[30] H. Pan, Y.W. Zhang, Edge-dependent structural, electronic and magnetic properties of MoS_2 nanoribbons, J. Mater. Chem. 22 (2012) 7280–7290.
[31] M.C. Lucking, J. Bang, H. Terrones, Y.Y. Sun, S.B. Zhang, Multivalency-induced band gap opening at MoS_2 edges, Chem. Mater. 27 (2015) 3326–3331.
[32] D. Dumcenco, D. Ovchinnikov, K. Marinov, et al., Large-area epitaxial monolayer MoS_2, ACS Nano 9 (2015) 4611.
[33] Lammps, http://lammps.sandia.gov.
[34] J.W. Jiang, H.S. Park, T. Rabczuk, Molecular dynamics simulations of single-layer molybdenum disulphide (MoS_2): Stillinger–Weber parametrization, mechanical properties, and thermal conductivity, J. Appl. Phys. 114 (2013) 064307.
[35] J.W. Jiang, Parametrization of Stillinger–Weber potential based on valence force field model: application to single-layer MoS_2 and black phosphorus, Nanotechnology 26 (2015) 315706.
[36] S. Xiong, G.X. Cao, Molecular dynamics simulations of mechanical properties of monolayer MoS_2, Nanotechnology 26 (2015) 1850752.
[37] K.Q. Dang, J.P. Simpsona, D.E. Spearot, Phase transformation in monolayer molybdenum disulphide (MoS_2) under tension predicted by molecular dynamics simulations, Scr. Mater. 76 (2014) 41–44.
[38] S.K. Singh, M. Neek-Amal, S. Costamagna, F.M. Peeters, Rippling, buckling, and melting of single-and multilayer MoS_2, Phys. Rev. B 91 (2015) 014101.
[39] T. Liang, S.R. Phillpot, S.B. Sinnott, Parametrization of a reactive many-body potential for Mo-S systems, Phys. Rev. B 79 (2009) 245110.
[40] A.K. Subramaniyan, C.T. Sun, Continuum interpretation of virial stress in molecular simulation, Int. J. Solids Struct. 45 (2008) 4340–4346.
[41] A. Stukowski, Visualization and analysis of atomistic simulation data with OVITO-the open visualization tool, Model. Simul. Mater. Sci. Eng. 18 (2010) 015012.
[42] J.S. Qi, X. Li, X.F. Qian, J. Feng, Bandgap engineering of rippled MoS_2 monolayer under external electric field, Appl. Phys. Lett. 102 (2013) 173112.
[43] P. Miró, M. Ghorbani-Asl, T. Heine, Spontaneous ripple formation in MoS_2 monolayers: electronic structure and transport effects, Adv. Mater. 25 (2015) 5473–5475.
[44] Y. Feruz, D. Mordehai, Towards a universal size-dependent strength of face-centered cubic nanoparticles, Acta Mater. 103 (2016) 433–441.
[45] A.J. Kulkarni, M. Zhou, K. Sarasamak, S. Limpijumnong, Novel phase transformation in ZnO nanowires under tensile loading, Phys. Rev. Lett. 97 (2006) 105502.
[46] J. Moon, M. Cho, M. Zhou, Size- and structure-dependence of thermal and mechanical behaviors of single crystalline and polytypic superlattice ZnS nanowires, J. Appl. Phys. 117 (2015) 214307.
[47] R. Rafael, C.G. Andrés, C. Emmanuele, G. Francisco, Strain engineering in semiconducting two-dimensional crystals, J. Phys.: Condens. Matter 27 (2015) 313201.
[48] T. Mandal, Strain induced phase transition in CdSe nanowires: effect of size and temperature, Appl. Phys. Lett. 101 (2012) 021906.
[49] A.N. Enyashin, I.R. Shein, A.L. Ivanovskii, Bending of MgO tubes: mechanically induced hexagonal phase of magnesium oxide, Phys. Rev. B 75 (2007) 245110.
[50] E. Cerda, K.R. Chandar, L. Mahadevan, Wrinkling of an elastic sheet under tension, Nature 419 (2002) 579–580.
[51] E. Cerda, L. Mahadevan, Geometry and physics of wrinkling, Phys. Rev. Lett. 90 (2003) 074302.
[52] Z. Wang, M. Devel, Periodic ripples in suspended graphene, Phys. Rev. B 83 (2011) 125422.
[53] L.Z. Kou, Y.D. Ma, S.C. Smith, C.F. Chen, Anisotropic ripple deformation in phosphorene, J. Phys. Chem. Lett. 6 (2015) 1509–1513.